Inorganic Chemistry

pubs.acs.org/IC

Article

Pressure–Temperature–Magnetic Field Phase Diagram of Multiferroic $(NH_4)_2FeCl_5{\cdot}H_2O$

Amanda J. Clune, Nathan C. Harms, Kevin A. Smith, Wei Tian, Zhenxian Liu, and Janice L. Musfeldt*

Cite This: *Inorg. Chem.* 2024, 63, 11021–11029

Read Online

ACCESS | Metrics & More | Article Recommendations | Supporting Information

ABSTRACT: We combined synchrotron-based infrared absorbance and Raman scattering spectroscopies with diamond anvil cell techniques and a symmetry analysis to explore the properties of multiferroic $(NH_4)_2FeCl_5{\cdot}H_2O$ under extreme pressure–temperature conditions. Compression-induced splitting of the Fe–Cl stretching, Cl–Fe–Cl and Cl–Fe–O bending, and NH_4^+ librational modes defines two structural phase transitions, and a group–subgroup analysis reveals space group sequences that vary depending upon proximity to the unexpectedly wide order–disorder transition. We bring these findings together with prior high-field work to develop the pressure–temperature–magnetic field phase diagram uncovering competing polar, chiral, and magnetic phases in this system.

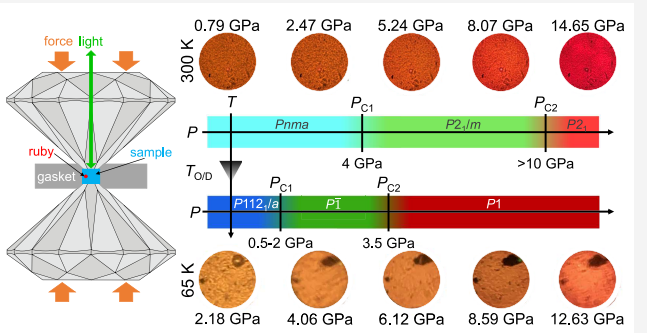

INTRODUCTION

Multiferroics are fascinating materials where ferroelectric and magnetic orders coexist, and spatial inversion and time-reversal symmetries are simultaneously broken.[1−14] Although challenging to realize, they offer foundational opportunities to investigate coupling across broad energy and time scales. These materials also hold promise for ultralow power memory and logic devices—if coupling is strong enough.[15−23] $(NH_4)_2[FeCl_5{\cdot}(H_2O)]$ is the multiferroic member of the $A_2[BX_5{\cdot}(H_2O)]$ family of erythrosiderites (A = K^+, Rb^+, NH_4^+; B = Fe^{3+}, Mn^{3+}, Co^{3+}; X = Cl^-, Br^-, H_2O). In this system, the $[FeCl_5(H_2O)]^{2-}$ groups are arranged in a herringbone-like pattern along the b-axis (Figure 1a). The overall structure is governed by an extensive network of intermolecular hydrogen and halogen bonding that holds the crystal together.[24−29] Ammonium fills the anion pocket and balances the charge. This system is magnetically complex with five unique but nearly iso-energetic exchange pathways (J_{1-5}) associated with various OH···Cl, NH···Cl, and Cl···Cl interactions.[24−26,28−30]

$(NH_4)_2[FeCl_5{\cdot}(H_2O)]$ displays a series of temperature-driven transitions including an order–disorder transition at 79 K,[31,32] antiferromagnetic ordering of the S = 5/2 Fe^{3+} centers below T_N = 7.25 K that creates collinear sinusoidal spin waves,[24,29] and ferroelectricity below T_C = 6.9 K that arises due to the development of an incommensurate-cycloidal spin state that coexists (and competes) with a commensurate distorted cycloidal phase.[29,33−35] Since magnetic ordering triggers ferroelectricity, $(NH_4)_2[FeCl_5{\cdot}(H_2O)]$ is a Type II system.[4] Multiferroicity in this regime arises from an inverse Dzyaloshinskii–Moriya mechanism in which the spin cycloid creates an electric polarization that breaks inversion symmetry.[10,36] Modeling of inelastic neutron scattering reveals that J_2 and J_4 are responsible for the cycloidal character of the spin waves.[35,37]

Under magnetic field, $(NH_4)_2[FeCl_5{\cdot}(H_2O)]$ undergoes a series of frustration-induced reorientations leading to a spin flop at 5 T.[29,38,39] Several high-field spin reorientations take place before the transition to the fully saturated magnetic state at H_{Sat} = 30 T (Figure 1).[38] Spin density calculations reveal how intermolecular interactions support magnetic exchange as well as changes in these pathways across the transition to the fully saturated state.[38] Electric polarization is similar to the magnetic response with a series of low-field polarization flops (from a to a' to c) across the spin flop transition[29,37,39] above which it grows linearly with increasing field,[37,40] reaching a maximum near 24 T before plunging to zero as the inversion center is lost near 27 T—consistent with expectations for a Type II multiferroic.[4,40] Multiferroicity in the commensurate quasi-collinear state above 5 T is described by the spin-dependent p–d hybridization model,[36] and recent work to 60 T shows that the system continues to display an orbital hybridization mechanism.[37,40] Therefore, $(NH_4)_2FeCl_5{\cdot}H_2O$ hosts two distinct magnetoelectric coupling mechanisms rather than a single overarching model. To the best of our knowledge,

Received: January 29, 2024
Revised: May 14, 2024
Accepted: May 17, 2024
Published: May 31, 2024

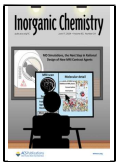

https://doi.org/10.1021/acs.inorgchem.4c00403
Inorg. Chem. 2024, 63, 11021–11029

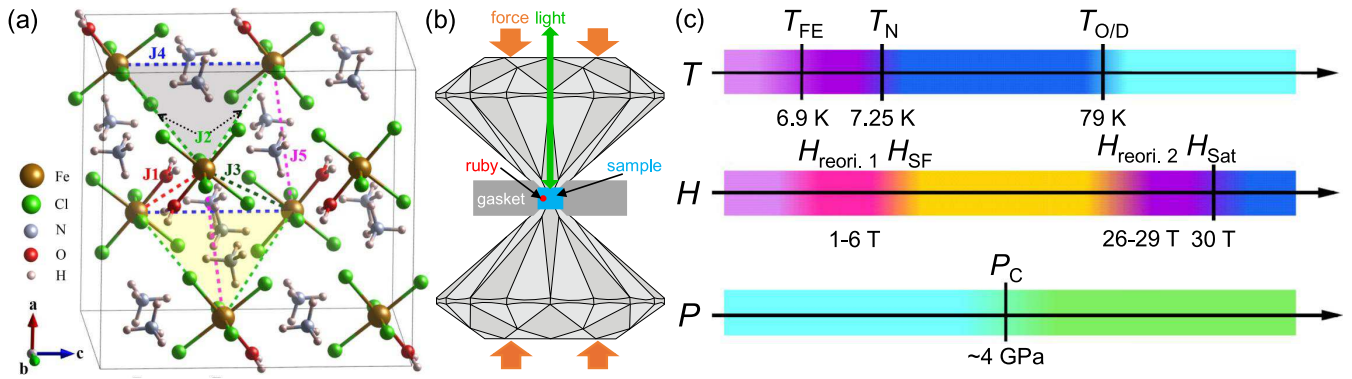

Figure 1. (a) Crystal structure of $(NH_4)_2FeCl_5{\cdot}H_2O$ at 300 K showing the five different magnetic exchange interactions (J_{1-5}). The latter are represented with colored dashed lines and are formed by intermolecular hydrogen and halogen bonding. The $[FeCl_5{\cdot}H_2O]^{2-}$ clusters create a herringbone-like chain down the *b*-axis with NH_4^+ ions in symmetrically equivalent positions to balance charge. (b) Schematic representation of the diamond anvil cell used for high-pressure vibrational spectroscopy. (c) Schematic summarizing the temperature-, magnetic field-, and pressure-induced transitions uncovered in this system thus far.

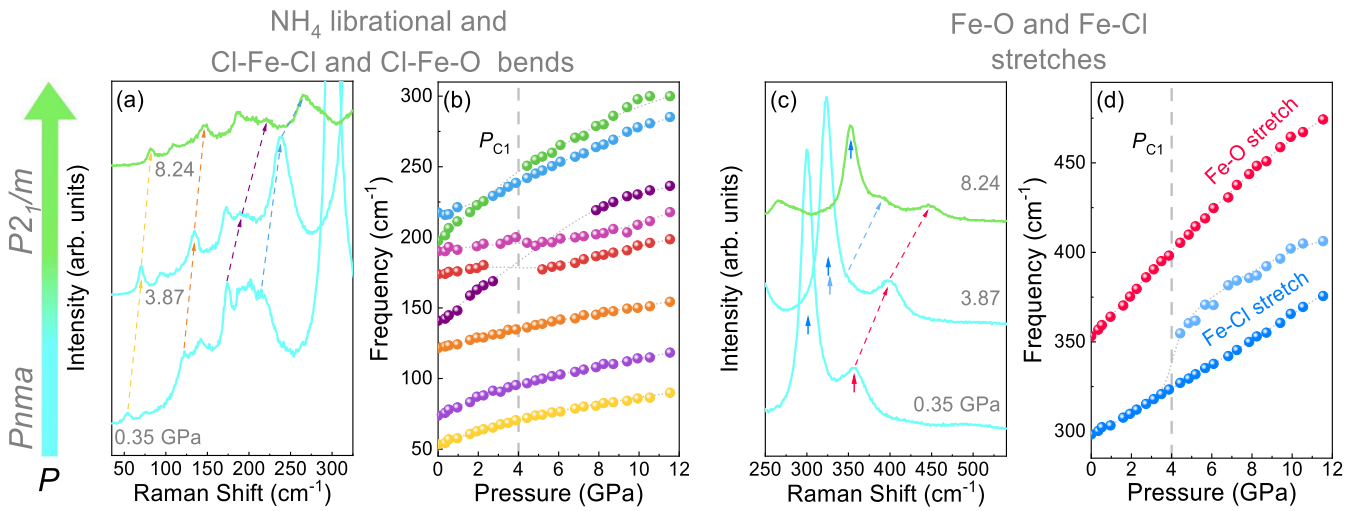

Figure 2. Close-up view of the Raman scattering response of $(NH_4)_2FeCl_5{\cdot}H_2O$ as a function of pressure at 300 K for (a) NH_4 librations and the Cl−Fe−Cl and Cl−Fe−O bending modes as well as (c) Fe−Cl stretching and Fe−O stretching modes. Splitting of the Fe−Cl stretch is an excellent signature of the 4 GPa structural phase transition ($P_{C,1}$). The arrows guide the eye. (b, d) Frequency vs pressure data for these data. Dotted lines guide the eye in panel (b). Error bars are on the order of the symbol size.

a magnetic field-dependent coupling mechanism has not been observed in any other multiferroic.

What differentiates $(NH_4)_2[FeCl_5{\cdot}(H_2O)]$ from other multiferroics such as $[(CH_3)_2NH_2]$ $Mn(HCOO)_3$[41] and the Ni analogue[42] is the fully molecular character of our target system, the fact that amine ordering does not immediately trigger ferroelectricity, and the manner in which intermolecular hydrogen and halogen bonding (rather than superexchange ligands) support magnetic interactions. As a result, $(NH_4)_2[FeCl_5{\cdot}(H_2O)]$ hosts exotic noncollinear magnetic states, a complex magnetic field−temperature phase diagram, and two different types of magnetoelectric coupling mechanisms in magnetic field as described above. Interestingly, metal−organic framework materials such as $[(CH_3)_2NH_2]$-$Mn(HCOO)_3$ and the Ni analogue sport pressure-driven polar phases at room temperature.[41,42] This capability is probably connected with their soft, flexible lattices. Whether a pressure-induced polar phase is accessible in $(NH_4)_2[FeCl_5{\cdot}(H_2O)]$ is an open question.

Inspired by the complex spin-charge interactions and the unique states of matter under a magnetic field, we combined synchrotron-based infrared absorbance and Raman scattering spectroscopies with diamond anvil cell techniques to reveal the properties of multiferroic $(NH_4)_2[FeCl_5{\cdot}(H_2O)]$ under extreme pressure−temperature conditions. We analyze the splitting pattern of the Fe−Cl stretching mode as well as trends in the Cl−Fe−Cl and Cl−FeO bending modes and NH_4^+ librations to uncover the critical pressures. Group−subgroup relationships allow us to unravel the symmetry progressions in both the high- and low-temperature phases. We bring these findings together with prior high-field data[29,38] to develop the pressure−temperature−magnetic field ($P-T-H$) phase diagram. By so doing, we untangle the relationships between different phases and reveal precisely how the polar space groups emerge under compression.

METHODS

$(NH_4)_2FeCl_5{\cdot}H_2O$ single crystals were grown by solution techniques as described previously.[29,33] The samples were loaded into diamond anvil cells equipped with either type IIa or low fluorescence diamonds. The culets ranged in size from 500 to 600 μm, and the gasket hole size was approximately 200 μm. We employed different pressure media depending upon the measurement: vacuum grease or KBr for infrared

https://doi.org/10.1021/acs.inorgchem.4c00403
Inorg. Chem. 2024, 63, 11021−11029

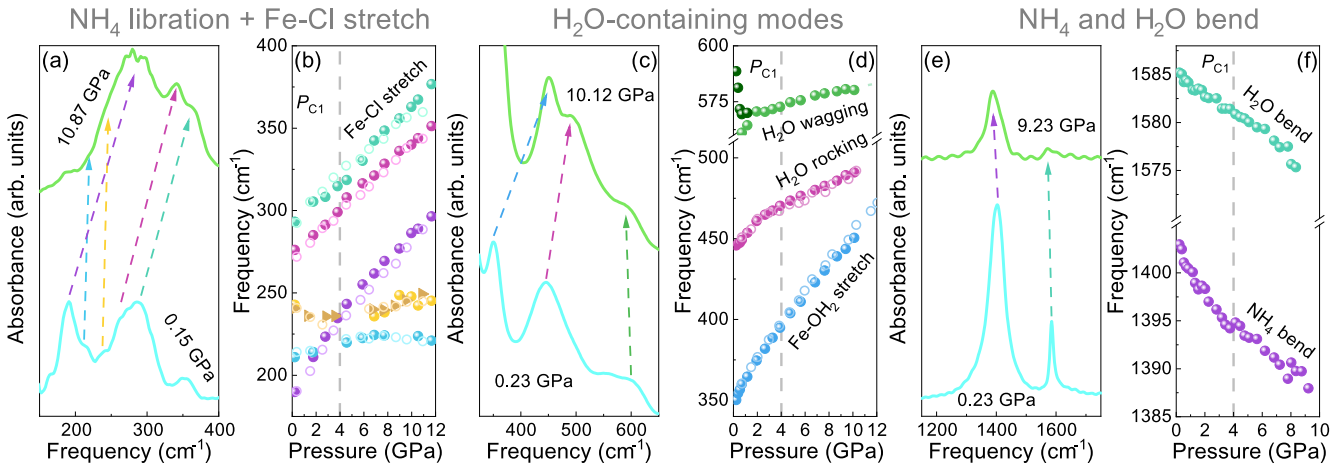

Figure 3. Close-up view of the infrared absorbance of $(NH_4)_2FeCl_5{\cdot}H_2O$ as a function of pressure at 300 K for (a) low-frequency libration modes and the Fe−Cl stretch, (c) H_2O-containing modes, and (e) NH_4 and H_2O bending modes. (b, d, f) Frequency vs pressure trends for these regions. Closed and open symbols in the frequency vs pressure plots are from two independent runs.

measurements and neat for Raman scattering. An annealed ruby ball was loaded into the cell with the sample and pressure medium, and the position of the *R*1 fluorescence was used to determine pressure.[43,44] In our case, the ruby lines remained sharp and well separated at all temperatures (Figure S1, Supporting Information) consistent with a quasi-hydrostatic environment.

High-pressure spectroscopic work was carried out at beamline 22-IR-1 at the National Synchrotron Light Source II, Brookhaven National Laboratory. Accelerator-based infrared spectra were collected using a Bruker 80v Fourier transform infrared spectrometer equipped with a liquid helium-cooled bolometer. These measurements covered the 50−8000 cm^{-1} range with 4 cm^{-1} resolution. Raman scattering measurements were performed between 40 and 650 cm^{-1} using both a 532 nm diode-pumped solid-state laser and a 646 nm red laser. We used <1 mW power, a 1200 g/mm grating, and a liquid nitrogen-cooled CCD detector. Each scan employed 60−90 s integration times, averaging as appropriate. We increased the pressure in small steps between 0 and approximately 15 GPa for room temperature work. For measurements under extreme pressure−temperature conditions, we loaded the diamond anvil cell into a custom-designed open-flow helium cryostat. Pressure was increased in situ from 0 to 10 GPa at each temperature of interest (from 300 K down to 35 K). Pressure was fully released after each temperature−pressure cycle, although because the system is not reversible, a fresh crystal was loaded for each measurement.

To complement this work, we performed variable temperature Raman scattering measurements under ambient pressure conditions using a Horiba Jobin-Yvon T64000 Raman spectrometer (25−500 cm^{-1}). This system was equipped with a 50× objective, 1800 g/mm grating, and a 532 nm laser. Laser power was kept below 1 mW to avoid sample damage. An open-flow helium cryostat provided temperature control. Standard peak fitting procedures were employed as appropriate.[45]

RESULTS AND DISCUSSION

Vibrational Response of $(NH_4)_2FeCl_5{\cdot}H_2O$ at Room Temperature. Figure 2 displays the Raman scattering response of $(NH_4)_2FeCl_5{\cdot}H_2O$ under compression at 300 K. The ambient pressure spectrum agrees well with prior results in terms of various peak positions and intensities,[46−48] although the high-pressure regime is completely unexplored. Our analysis focuses primarily on the NH_4^+ librations, the Cl−Fe−Cl and O−Fe−Cl bends, and the Fe−Cl and Fe−OH_2 stretches. These features are assigned using first-principles lattice dynamics calculations, $K_2FeCl_5{\cdot}H_2O$ analogue data, neutron scattering results, and literature data showing typical librations of H_2O and NH_4^+.[49−53] Our assignments are summarized in the Supporting Information (Table S1).

The frequency vs pressure trends in Figure 2b,d reveal the local lattice distortions and associated critical pressures. As always, we use peak appearances or disappearances, splittings or recombinations, and slope changes to identify critical pressures. The Fe−Cl stretching mode near 300 cm^{-1} is a good example. This feature begins as a single peak, forms a small shoulder immediately below 4 GPa, and becomes a clear doublet above 4 GPa. Splitting of the Fe−Cl stretching mode signals the development of a distorted Fe environment in the $[FeCl_5{\cdot}H_2O]^{2-}$ polyhedra involving the chloride ligands, which changes the space group from *Pnma*[29,31] to one of lower symmetry. We use this doublet splitting to define a critical pressure (P_{C1}) of 4 GPa at 300 K. The Fe−OH_2 stretching mode near 350 cm^{-1} is different. It does not split across P_{C1}. Instead, it hardens systematically under compression. The Cl−Fe−Cl and O−Fe−Cl bending modes as well as the NH_4^+ librations also harden systematically under pressure at room temperature with no evidence for symmetry changes up to 15 GPa.

For completeness, we also measured the synchroton-based infrared absorbance under compression (Figure 3). The ambient pressure spectrum of $(NH_4)_2FeCl_5{\cdot}H_2O$ at 300 K is in excellent agreement with earlier studies,[48,54,55] although again the high pressure response is completely unexplored. Our mode assignments are summarized in the Supporting Information (Table S2). The features of interest include the low-frequency libration modes, Fe−Cl stretch, H_2O-containing motions (stretching, rocking, wagging, and bending), and the NH_4^+ bending modes. In the infrared, the Fe−Cl stretching vibration does not split with increasing pressure as in the Raman scattering response. (This is because symmetry is odd rather than even.) Instead, the peak position increases systematically under compression, in line with the behavior of the Fe−OH_2 stretch. The opposite is seen for the H_2O and NH_4^+ bending modes; compression causes mode softening. This trend is consistent with improved hydrogen bonding or a change in orientation as seen in $C_2H_6N_4O_2$ and $NH_2SO_2NH_2$.[56,57] In this case, mode softening provides direct microscopic proof of enhanced hydrogen and halogen

https://doi.org/10.1021/acs.inorgchem.4c00403
Inorg. Chem. 2024, 63, 11021−11029

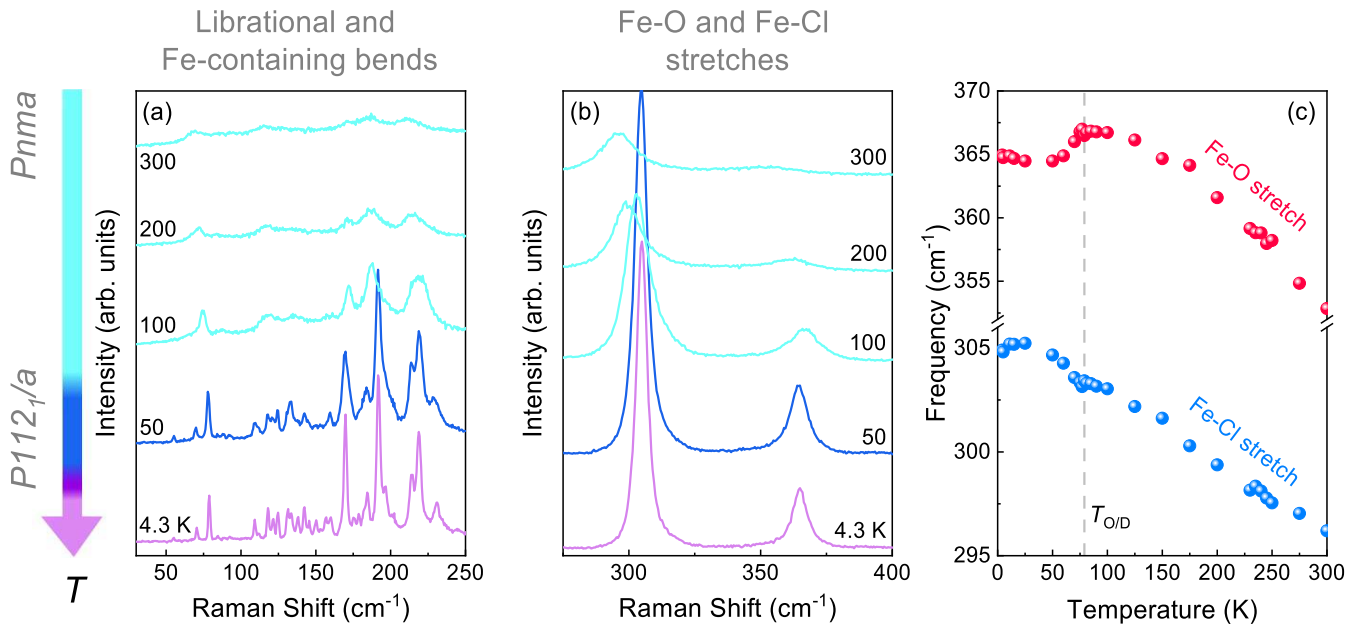

Figure 4. Variable temperature Raman scattering response of $(NH_4)_2FeCl_5{\cdot}H_2O$ across the order−disorder transition highlighting the (a) low-frequency NH_4 librations, the Cl−Fe−Cl and Cl−Fe−O bending modes, and (b) Fe−Cl and Fe−O stretching modes. (c) Frequency vs temperature plot emphasizing changes across $T_{O/D}$ = 79 K. Ordering of the ammonium ion begins at 79 K and continues until approximately 50 K, creating a wide dynamic range for the ordering process. These data were collected at ambient pressure.

bonding. Stronger intermolecular bonding will enhance the associated superexchange pathways (Fe−O−H···Cl−Fe, Fe−Cl···Cl−Fe, and Fe−Cl···O−Fe linkages).

In the remainder of this work, we focus on the Raman scattering response of $(NH_4)_2FeCl_5{\cdot}H_2O$ under compression because the Fe−Cl stretching mode shows the development of a clear doublet across P_{C1} = 4 GPa. This makes the position of the structural phase transition very easy to identify.

$(NH_4)_2FeCl_5{\cdot}H_2O$ across the 79 K Order−Disorder Transition. Although the room temperature *Pnma* space group is well-known,[31,54] the crystal structure of $(NH_4)_2FeCl_5{\cdot}H_2O$ below the order−disorder transition has been challenging to resolve. Rodriguez et al. and Brüning et al. independently studied the structure across the order−disorder temperature, although there are still a number of inconsistencies.[31,52] Depending on the measurement, crystal symmetries of either *Pnma* or $P112_1/a$ were identified at 45 and 50 K, respectively. Even at 2 K, the system was reported to host $P112_1/a$ symmetry.[31] Importantly, the authors did not perform additional systematic measurements between 50 and 2 K. $P112_1/a$ also contains a center of inversion. We can draw two main conclusions based upon prior X-ray data: (i) $P112_1/a$ is at least consistent with the properties of $(NH_4)_2FeCl_5{\cdot}H_2O$ above T_{FE} = 6.9 K since the material has no polarization at these temperatures, and (ii) the $P112_1/a$ space group can not be valid below the ferroelectric transition because the development of a polar state requires loss of the inversion center. Additional information is available to help resolve this problem. Recent specific heat and polarization measurements carried out on mixed erythrosiderite $[(NH_4)_{(1-x)}K_x]_2FeCl_5{\cdot}H_2O$ reveal (i) that $T_{O/D}$ is related to the ordering of the ammonium ion and (ii) there is no measurable polarization in the pure compound across the order−disorder temperature.[52] It is therefore evident that symmetry is reduced from *Pnma* → $P112_1/a$ across the order−disorder transition, although the space group of $(NH_4)_2FeCl_5{\cdot}H_2O$ below the magnetic and ferroelectric transitions remains unknown. Of course, it must be a polar subgroup of $P112_1/a$.

Vibrational spectroscopy can help uncover the low-temperature space group. Figure 4 displays the Raman scattering response of $(NH_4)_2FeCl_5{\cdot}H_2O$ as a function of temperature. In the high-temperature phase, frequency vs temperature trends are simple with standard anharmonic hardening with decreasing temperature. Distinct spectral changes begin to appear across the order−disorder transition ($T_{O/D}$ = 79 K), although a detailed fine structure develops fully only below 50 K. This creates a broad dynamic temperature range between 79 and approximately 50 K over which the free ammonium ion and water ligand order, triggering the development of additional hydrogen bonding interactions. Since these low-frequency modes are associated with NH_4^+ librations and Cl−Fe−Cl + Cl−Fe−O bending motions, peak splitting signifies a lower symmetry space group. These low-frequency features could also contain ferroelectric modes below 6.9 K, but careful examination reveals no obvious candidates (Figure S6). This makes sense because polar modes have odd rather than even symmetry and are infrared-active. We emphasize that the Raman-active Fe−Cl stretching mode does not split with decreasing temperature. This observation indicates that the symmetry and space group of $(NH_4)_2FeCl_5{\cdot}H_2O$ in the low-temperature phase does not resemble that above P_{C1} = 4 GPa (Figure 2). A full set of frequency vs temperature plots can be found in the Supporting Information (Figure S5).

Tracking the Fe−Cl Stretching Mode as a Function of Pressure and Temperature. Figure 5 summarizes the Raman scattering response of the Fe−Cl stretching mode as a function of pressure at a few different temperatures above and below the 79 K order−disorder transition. Spectra collected at 250 K are very similar to those at room temperature; the Fe−Cl feature splits into a strong doublet with increasing pressure across P_{C1}. The behavior changes as temperature drops. At 150 K, the Fe−Cl stretching mode

https://doi.org/10.1021/acs.inorgchem.4c00403
Inorg. Chem. 2024, 63, 11021−11029

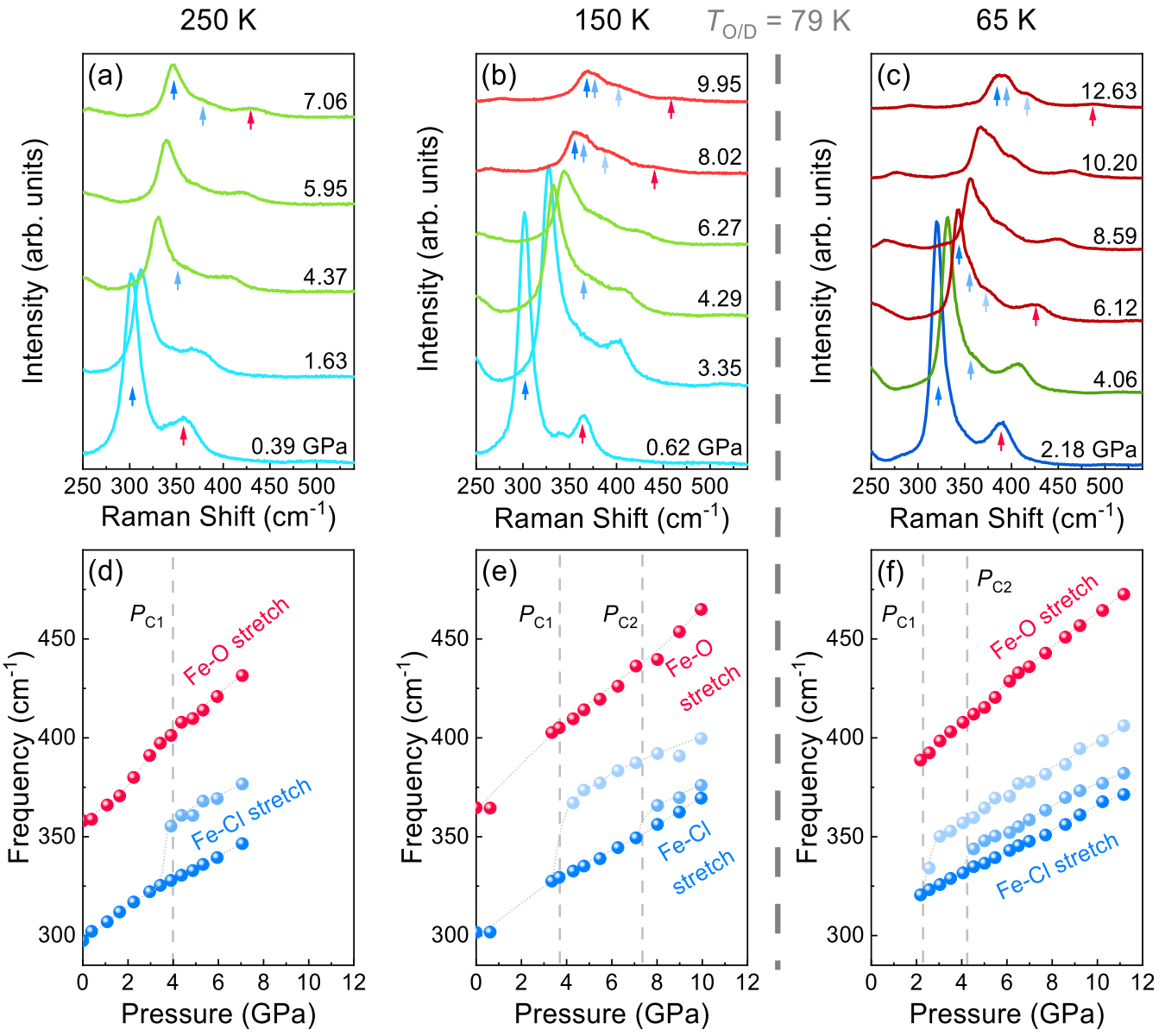

Figure 5. Close-up view of the Raman-active Fe−Cl and Fe−OH_2 stretching modes as a function of pressure. (a, b) Spectra taken above the order−disorder temperature at 250 and 150 K and (d, e) their corresponding frequency vs pressure plots. (c, f) Raman spectra collected at 65 K and the corresponding frequency vs pressure trends. The latter is below the 79 K order−disorder transition.

reveals triplet character under compression, and two critical pressures are observed (Figure 5b,e). We find P_{C1} = 3.7 GPa and P_{C2} = 7.5 GPa. Below $T_{O/D}$, both P_{C1} and P_{C2} decrease significantly—a direct result of NH_4^+ ordering. Additional low-frequency features also arise, similar to those found in the low-temperature Raman scattering response of $(NH_4)_2FeCl_5{\cdot}H_2O$ at ambient pressure (Figure 4). However, when pressure is applied, symmetry is reduced, and a new space group develops. The Fe−Cl linkages are directly associated with the symmetry of the Fe polyhedron, the various exchange pathways, and hydrogen bonding to neighboring ammonia ions. Changes in the Fe−Cl stretching mode demonstrate that compression drives $(NH_4)_2FeCl_5{\cdot}H_2O$ into two completely new phases. Both symmetry reduction sequences will be discussed below.

Symmetry Analysis of the High-Pressure Phases in $(NH_4)_2FeCl_5{\cdot}H_2O$. $(NH_4)_2[FeCl_5{\cdot}(H_2O)]$ undergoes a series of pressure-driven symmetry progressions that depend upon proximity to the unexpectedly broad 79 K order−disorder transition (Figure 5). This creates two separate cases for us to examine: (i) the progression in the high-temperature phase beginning with *Pnma* and (ii) the progression in the low-temperature phase starting with $P112_1/a$. In each case, $(NH_4)_2[FeCl_5{\cdot}(H_2O)]$ is driven through two critical pressures although to completely different high-pressure space groups.

Figure 6 displays the subgroup tree that we will use to analyze the pressure-driven symmetry progressions.[58−60] The subgroup tree of *Pnma* is complex; however, it is much smaller and simpler for $P112_1/a$. We therefore elect to solve the low-temperature phase symmetry progression first. As a reminder, decreasing temperature across the order−disorder transition reduces the space group from *Pnma* → $P112_1/a$, and the system loses symmetry in the form of (i) a 2-fold screw axis with the inversion center, (ii) a mirror plane, and (iii) a diagonal glide. This process is indicated with the purple arrow in Figure 6. The low-temperature $P112_1/a$ phase undergoes two transitions that reflect how the Fe−Cl stretching, Cl−Fe−

https://doi.org/10.1021/acs.inorgchem.4c00403
Inorg. Chem. 2024, 63, 11021−11029

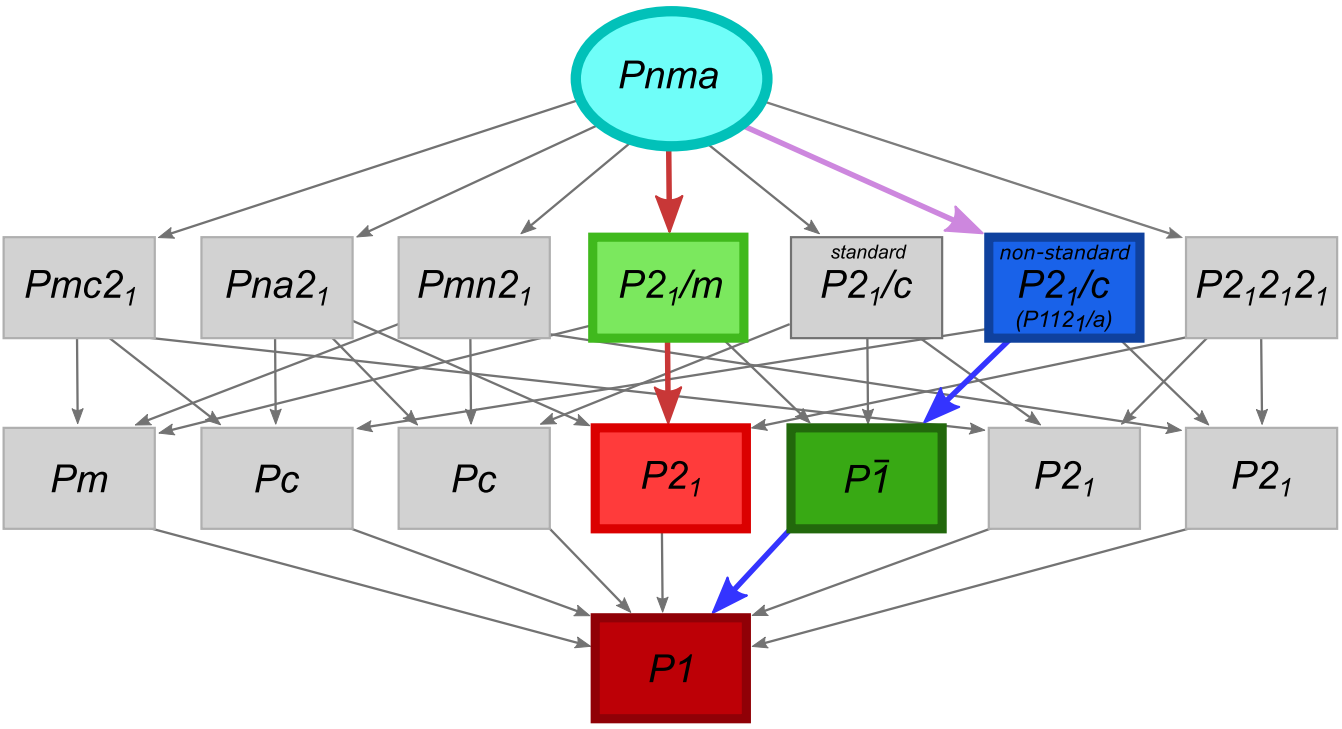

Figure 6. Schematic representation of the symmetry tree for $(NH_4)_2FeCl_5{\cdot}H_2O$. Here, *Pnma* is the high-temperature space group. $P112_1/a$, which is a nonstandard subset of $P2_1/c$, is the low-temperature space group. The high- to low-temperature phase transition is indicated by the purple arrow. Both can be driven to lower symmetry with pressure. Their sequential pathways are highlighted in red and blue, respectively.

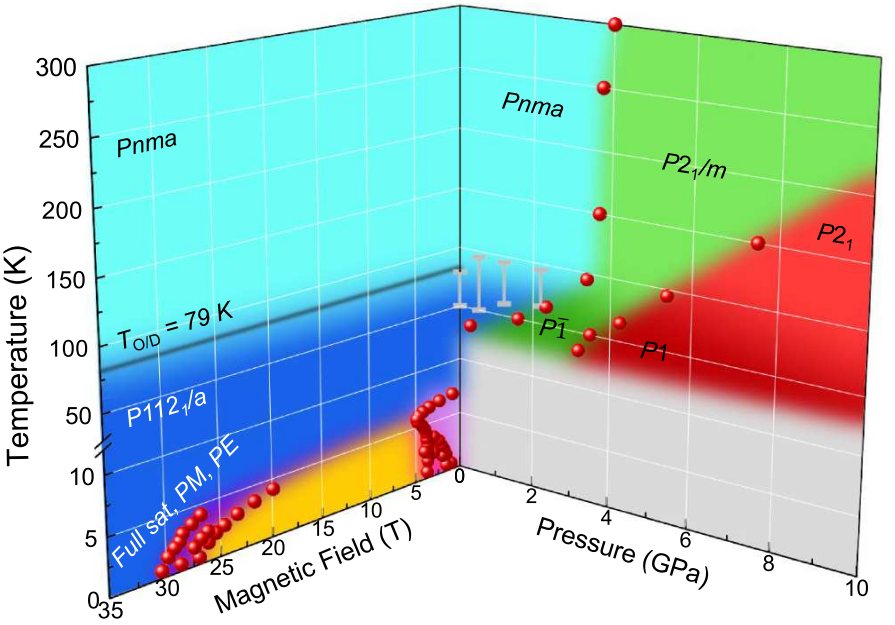

Figure 7. $P{-}T{-}H$ phase diagram of multiferroic $(NH_4)_2FeCl_5{\cdot}H_2O$. The space groups are labeled. Extrapolating $P_{C,2}$ to room temperature, we expect to find the polar + chiral $P2_1$ phase just above 15 GPa. As shown by the gray bars, $\partial T_{O/D}/\partial P$ is slightly positive as discussed in the Supporting Information. The gray areas on the phase diagram are inaccessible in our experiments.

Cl + Cl−Fe−O bending, and NH_4^+ librational modes break symmetry under compression. These pressure-induced distortions are along the herringbone-like chains in $(NH_4)_2[FeCl_5{\cdot}(H_2O)]$. This creates a distortion along the chains that breaks the 2-fold screw axis and axial glide while maintaining the inversion center ($P112_1/a \rightarrow P\bar{1}$) as evidenced by the splitting of the Fe−Cl stretch (Figures 2 and 5) and the Cl−Fe−Cl and Cl−Fe−O bending modes (Figure S7). The only space group in Figure 6 with symmetry lower than $P\bar{1}$ is *P*1, so the logical space group candidate above the second critical pressure is *P*1. This critical pressure marks the point where the Fe−Cl stretching mode displays triplet character and the Fe-containing bending modes split for a second time. These fine structures indicate that the Fe polyhedron is highly distorted, and the center of inversion is lost. Thus, the low-

https://doi.org/10.1021/acs.inorgchem.4c00403
Inorg. Chem. 2024, 63, 11021−11029

temperature space group sequence goes as $P112_1/a \rightarrow P\bar{1} \rightarrow P1$. Note that $P1$ is a polar space group.

The situation is more complex above the order−disorder transition. It can be resolved using our knowledge of the space group progression in the low-temperature phase and comparing it with spectra in the different phases to assess a match (or not). The high-temperature pathway begins at *Pnma* and can include a number of lower symmetry space group candidates including $Pmc2_1$, $Pna2_1$, $Pmn2_1$, $P2_1/m$, $P2_1/c$ (standard setting), $P2_1/c$ (nonstandard setting), or $P2_12_12_1$. Our understanding of the relationships between the low-temperature space groups is useful for eliminating some candidates. Above the order−disorder transition, we know that *Pnma* is driven to an unknown space group. If this unknown space group is lowered in temperature across $T_{O/D}$, it should transform to $P\bar{1}$—which resides at low temperature and high pressure. Thus, *Pnma* must be driven to a space group that can also lower symmetry to the $P\bar{1}$ phase. This eliminates numerous candidates and leaves $P2_1/m$, $P2_1/c$, and $P2_1/c$. Additionally, the high-pressure spectra above $T_{O/D}$ do not resemble those in the low-temperature space group, which eliminates both standard and nonstandard $P2_1/c$ candidates. This leaves $P2_1/m$ as the only remaining space group, so the symmetry lowers as $Pnma \rightarrow P2_1/m$, implying that (i) a 2-fold screw axis, (ii) a diagonal glide, and (iii) an axial glide are lost. The last remaining transition is associated with Pm, $P2_1$, or $P\bar{1}$. Again, $P\bar{1}$ is easily eliminated because this phase does not resemble the low-temperature spectra that have already been assigned to $P\bar{1}$. The remaining two space groups are distinguished by whether a mirror plane or a 2-fold screw axis remains under pressure. However, the transition from $P2_1/m \rightarrow Pm$ would require the mirror plane to shift its location within the unit cell and is less likely to occur. If a mirror plane was repositioned, we would expect additional low-frequency features to arise. This is not the case, as evidenced by the data in Figure 2. We therefore conclude that Pm is not the correct high-pressure space group either. This leaves only $P2_1$. Thus, the room temperature space group progression likely goes as $Pnma \rightarrow P2_1/m \rightarrow P2_1$ under compression. Again $P2_1$ is a polar space group. It is also chiral.

Developing the Phase Diagram of $(NH_4)_2[FeCl_5\cdot(H_2O)]$. Figure 7 displays the pressure−temperature ($P-T$) phase diagram of $(NH_4)_2FeCl_5\cdot H2O$ created from our spectroscopic data. There are numerous phase boundaries both above and below the 79 K order−disorder transition. Focusing first on the high-temperature properties, we see that P_{C1} defines the $Pnma \rightarrow P2_1/m$ transition. These space groups are indicated on the phase diagram. P_{C2} is not observed at room temperature—at least not below 15 GPa—although it does appear as temperature decreases. P_{C1} remains near 4 GPa as the temperature drops, shifting downward on the approach to the order−disorder transition. This phase boundary continues to shift to lower pressure below $T_{O/D}$, forming a nexus of activity between 79 and 50 K that eventually quenches P_{C1}, both explaining the complexity of our variable temperature spectroscopic results (Figure 4) and making the crystal structure challenging to resolve.[31,54] Below $T_{O/D}$, the space group sequence is $P112_1/a \rightarrow P\bar{1} \rightarrow P1$. The $P2_1/m$ and $P\bar{1}$ phases, indicated in light and dark green, narrow significantly as temperature decreases. The high-pressure phases ($P2_1$ and $P1$) are polar both above and below $T_{O/D}$; $P2_1$ is also chiral. At the present time, it is not known whether polarization is switchable (ferroelectric) or not (pyroelectric). It is also not known how T_N and T_C evolve under compression. Given the crucial role of the Fe−Cl stretch, Cl−Fe−Fl and O−Fe−Cl bends, and NH_4^+ librational modes in the series of structural phase transitions, we hypothesize that similar interactions will impact the magnetic exchange pathways and the development of low-temperature polarization.

Bringing these results together with prior high field magnetization,[29,38] we can develop the pressure−temperature−magnetic field ($P-T-H$) phase diagram of $(NH_4)_2FeCl_5\cdot H_2O$ (Figure 7). Looking at the $T-H$ plane, we find the spin flop, a transition to the fully saturated spin state, and various additional reorientational transitions associated with the different magnetic exchange interactions.[29,38] We therefore see that both field- and pressure-induced transitions involve the Fe−O and Fe−Cl bonds but in different ways. These ultralow symmetry phases are accessible with experimentally realizable pressures and magnetic fields, both of which deliver deterministic property control.

SUMMARY

The molecular multiferroic $(NH_4)_2[FeCl_5\cdot(H_2O)]$ hosts an extensive network of hydrogen and halogen bonds, two independent magnetoelectric coupling mechanisms, and a complex hierarchy of competing phases—characteristics that distinguish it from more well-studied counterparts such as the metal−organic frameworks. While $[(CH_3)_2NH_2]Mn(HCOO)_3$ and the Ni analogue have been explored under pressure,[41,42] there have been no comprehensive studies of how pressure leads to the development of new states of matter in multiferroics where the crystals are held together by intermolecular hydrogen and halogen bonds. To address these questions, we combined synchrotron-based infrared absorbance and Raman scattering spectroscopies with diamond anvil cell techniques to investigate the high-pressure properties of this unusual material. Our primary findings include (i) revealing a set of pressure-driven structural distortions and (ii) teasing out the symmetry progression under compression in the high- and low-temperature phases. The aforementioned symmetry analysis made use of the displacement patterns from our lattice dynamics calculations as well as Landau theory of group−subgroup relations for phase transitions. This strategy works because the irreducible representations of a space group are unique characteristics of that space group. Bringing our spectroscopic results together, we generate the pressure−temperature−magnetic field phase diagram for multiferroic $(NH_4)_2FeCl_5H_2O$. In addition to untangling the relationships between competing phases, symmetry arguments suggest that the high-pressure phases are polar—irrespective of proximity to the 79 K order−disorder transition. We therefore see that pressurizing a soft material can foster ferroelectricity in unexpected parts of $P-T$ space and, at the same time, promote enhanced polarization under compression.[61] Whether other molecular multiferroics host easily accessible high-pressure polar phases is an open question that merits further investigation.

ASSOCIATED CONTENT

Supporting Information

The Supporting Information is available free of charge at https://pubs.acs.org/doi/10.1021/acs.inorgchem.4c00403.

Ruby fluorescence spectra as a function of temperature and pressure revealing quasi-hydrostatic conditions,

https://doi.org/10.1021/acs.inorgchem.4c00403
Inorg. Chem. 2024, 63, 11021−11029

summary of vibrational mode assignments including symmetries, example of how critical pressures are determined, complete summary of the variable temperature Raman scattering results, complete summary of the synchrotron infrared absorbance as a function of pressure, close-up view of the Raman scattering response above and below the ferroelectric transition, and summary of our complementary Raman work using a red (rather than green) laser (PDF)

AUTHOR INFORMATION

Corresponding Author

Janice L. Musfeldt − *Department of Chemistry and Department of Physics and Astronomy, University of Tennessee, Knoxville, Tennessee 37996, United States;* orcid.org/0000-0002-6241-823X; Email: musfeldt@utk.edu

Authors

Amanda J. Clune − *Department of Chemistry, University of Tennessee, Knoxville, Tennessee 37996, United States;* orcid.org/0000-0001-8618-1700

Nathan C. Harms − *Department of Chemistry, University of Tennessee, Knoxville, Tennessee 37996, United States;* orcid.org/0000-0002-2600-825X

Kevin A. Smith − *Department of Chemistry, University of Tennessee, Knoxville, Tennessee 37996, United States*

Wei Tian − *Neutron Scattering Division, Oak Ridge National Laboratory, Oak Ridge, Tennessee 37831, United States*

Zhenxian Liu − *Department of Physics, University of Illinois Chicago, Chicago, Illinois 60607-7059, United States*

Complete contact information is available at: https://pubs.acs.org/10.1021/acs.inorgchem.4c00403

Notes

The authors declare no competing financial interest.
Standard laser safety protocols should be followed carefully.

ACKNOWLEDGMENTS

Research at the University of Tennessee is supported by Chemical Structure and Dynamics, Division of Chemistry, National Science Foundation (CHM-2342425). Work at ORNL is funded by the U.S. Department of Energy, Office of Science, Basic Energy Sciences, Materials Sciences and Engineering Division, Condensed Matter Experiment and Theory Programs. Work at the National Synchrotron Light Source II at Brookhaven National Laboratory is funded by the Department of Energy (DE-AC98-06CH10886). Use of the 22-IR-1 beamline is supported by the National Science Foundation—Earth Sciences via SEES: Synchrotron Earth and Environmental Science (EAR − 2223273) and CDAC (DE-NA0003975). We thank J. Fernandez-Baca and R. S. Fishman for useful conversations.

REFERENCES

(1) Hill, N. A. Why are there so few magnetic ferroelectrics? *J. Phys. Chem. B* **2000**, *104*, 6694−6709.
(2) Spaldin, N. A.; Fiebig, M. The renaissance of magnetoelectric multiferroics. *Science.* **2005**, *309*, 391−392.
(3) Cheong, S.-W.; Mostovoy, M. Multiferroics: a magnetic twist for ferroelectricity. *Nat. Mater.* **2007**, *6*, 13−20.
(4) Khomskii, D. Classifying multiferroics: mechanisms and effects. *Physics* **2009**, *2*, 20.
(5) Weng, D.-F.; Wang, C.-M.; Gao, S. Framework-structured weak ferromagnets. *Chem. Soc. Rev.* **2011**, *40*, 3157−3181.
(6) Benedek, N. A.; Fennie, C. J. Hybrid improper ferroelectricity: A mechanism for controllable polarization-magnetization coupling. *Phys. Rev. Lett.* **2011**, *106*, No. 107204.
(7) Pardo, E.; Train, C.; Liu, H.; Chamoreau, L.-M.; Dkhil, B.; Boubekeur, K.; Lloret, F.; Nakatani, K.; Tokoro, H.; Ohkoshi, S. I.; Verdaguer, M. Multiferroics by rational design: implementing ferroelectricity in molecule-based magnets. *Angew. Chemie - Int. Ed.* **2012**, *51*, 8356−8360.
(8) Zhang, J. T.; Lu, X. M.; Zhou, J.; Sun, H.; Su, J.; Ju, C. C.; Huang, F. Z.; Zhu, J. S. Origin of magnetic anisotropy and spiral spin order in multiferroic $BiFeO_3$. *Appl. Phys. Lett.* **2012**, *100*, No. 242413.
(9) Di Sante, D.; Stroppa, A.; Jain, P.; Picozzi, S. Tuning the ferroelectric polarization in a multiferroic metal-organic framework. *J. Am. Chem. Soc.* **2013**, *135*, 18126−18130.
(10) Tokura, Y.; Seki, S.; Nagaosa, N. Multiferroics of spin origin. *Rep. Prog. Phys.* **2014**, *77*, No. 076501.
(11) Peng, J.; Zhang, Y.; Lin, L. F.; Lin, L.; Liu, M.; Liu, J. M.; Dong, S. New iron-based multiferroics with improper ferroelectricity. *J. Phys. D. Appl. Phys.* **2018**, *51*, No. 243002.
(12) Spaldin, N. A.; Ramesh, R. Advances in magnetoelectric multiferroics. *Nat. Mater.* **2019**, *18*, 203−212.
(13) Chikara, S.; Gu, J.; Zhang, X. G.; Cheng, H. P.; Smythe, N.; Singleton, J.; Scott, B.; Krenkel, E.; Eckert, J.; Zapf, V. S. Magnetoelectric behavior via a spin state transition. *Nat. Commun.* **2019**, *10*, 4043.
(14) Ma, Y.; Sun, Y. Multiferroic and thermal expansion properties of metal-organic frameworks. *J. Appl. Phys.* **2020**, *127*, No. 080901.
(15) Béa, H.; Gajek, M.; Bibes, M.; Barthélémy, A. Spintronics with multiferroics. *J. Phys.: Condens. Matter* **2008**, *20*, No. 434221.
(16) Bibes, M.; Barthélémy, A. Multiferroics: Towards a magnetoelectric memory. *Nat. Mater.* **2008**, *7*, 425−426.
(17) Parkin, S. S. P.; Hayashi, M.; Thomas, L. Magnetic Domain-Wall Racetrack Memory. *Science (80-.)* **2008**, *320*, 190−194.
(18) Baek, S. H.; Jang, H. W.; Folkman, C. M.; Li, Y. L.; Winchester, B.; Zhang, J. X.; He, Q.; Chu, Y. H.; Nelson, C. T.; Rzchowski, M. S.; Pan, X. Q.; Ramesh, R.; Chen, L. Q.; Eom, C. B. Ferroelastic switching for nanoscale non-volatile magnetoelectric devices. *Nat. Mater.* **2010**, *9*, 309−314.
(19) Prins, F.; Monrabal-Capilla, M.; Osorio, E. A.; Coronado, E.; Van Der Zant, H. S. Room-temperature electrical addressing of a bistable spin-crossover molecular system. *Adv. Mater.* **2011**, *23*, 1545−1549.
(20) Catalan, G.; Seidel, J.; Ramesh, R.; Scott, J. F. Domain wall nanoelectronics. *Rev. Mod. Phys.* **2012**, *84*, 119−156.
(21) Nikonov, D. E.; Young, I. A. Benchmarking of Beyond-CMOS Exploratory Devices for Logic Integrated Circuits. *IEEE J. Explor. Solid-State Comput. Devices Circuits* **2015**, *1*, 3−11.
(22) Mittal, S. A survey of techniques for architecting processor components using domain-wall memory. *ACM J. Emerg. Technol. Comput. Syst.* **2016**, *13*, 29 DOI: 10.1145/2994550.
(23) Yang, S.-H. Spintronics on chiral objects. *Appl. Phys. Lett.* **2020**, *116*, No. 120502.
(24) McElearney, J. N.; Merchant, S. Nonisomorphic antiferromagnetic behavior of two isomorphic salts: low-temperature heat capacities and magnetic susceptibilities of $(NH_4)_2FeCl_5{\cdot}H_2O$ and $K_2FeCl_5{\cdot}H_2O$. *Inorg. Chem.* **1978**, *17*, 1207−1215.
(25) Schultz, A. J.; Carlin, R. L. Single-crystal pulsed neutron diffraction structure of the antiferromagnet K2[FeCl5(H2O)] with and without applied pressure. *Acta Crystallogr. Sect. B* **1995**, *51*, 43−47.
(26) Figgis, B. N.; Raston, C. L.; Sharma, R. P.; White, A. H. Crystal structure of diammonium aquapentachloroferrate(III). *Aust. J. Chem.* **1978**, *31*, 2717−2720.
(27) Gabás, M.; Palacio, F.; Rodríguez-Carvajal, J.; Visser, D. Magnetic structures of the three-dimensional Heisenberg antiferromagnets $K_2FeCl_5{\cdot}D_2O$ and $Rb_2FeCl_5{\cdot}D_2O$. *Phys. Rev. B* **1995**, *7*, 4725.

(28) Campo, J.; Luzón, J.; Palacio, F.; McIntyre, G. J.; Millán, A.; Wildes, A. R. Understanding magnetic interactions in the series $A_2FeX_5{\cdot}H_2O$ (A = K, Rb; X = Cl, Br). II. Inelastic neutron scattering and DFT studies. *Phys. Rev. B* **2008**, *78*, No. 054415.
(29) Ackermann, M.; Brüning, D.; Lorenz, T.; Becker, P.; Bohatý, L. Thermodynamic properties of the new multiferroic material $(NH_4)_2FeCl_5{\cdot}H_2O$. *New J. Phys.* **2013**, *15*, No. 123001.
(30) Gómez-Aguirre, L. C.; Pato-Doldán, B.; Mira, J.; Castro-García, S.; Senarís-Rodríguez, M. A.; Sánchez-Andújar, M.; Singleton, J.; Zapf, V. S. Magnetic ordering-induced multiferroic behavior in $[CH_3NH_3]$-$[Co(HCOO)_3]$ metal-organic framework. *J. Am. Chem. Soc.* **2016**, *138*, 1122−1125.
(31) Rodríguez-Velamazán, J. A.; Fabelo, O.; Millán, A.; Campo, J.; Johnson, R. D.; Chapon, L. Magnetically-induced ferroelectricity in the $(ND_4)_2[FeCl_5(D_2O)]$ molecular compound. *Sci. Rep.* **2015**, *5*, 14475.
(32) Canadillas-delgado, L.; Fabelo, O.; Rodríguez-Velamazán, J. A.; Lemée-Cailleau, M.-H.; Mason, S. A.; Pardo, E.; Lloret, F.; Zhao, J.-P.; Bu, X.-H.; Simonet, V.; Colin, C. V.; Rodríguez-Carvajal, J. The role of order-disorder transitions in the quest for molecular multiferroics: structural and magnetic neutron studies of a mixed valence iron(II)-iron(III) formate framework. *J. Am. Chem. Soc.* **2012**, *134*, 19772−19781.
(33) Tian, W.; Cao, H.; Wang, J.; Ye, F.; Matsuda, M.; Yan, J.-Q.; Liu, Y.; Garlea, V. O.; Agrawal, H. K.; Chakoumakos, B. C.; Sales, B. C.; Fishman, R. S.; Fernandez-Baca, J. A. Spin-lattice coupling mediated multiferroicity in $(ND_4)_2FeCl_5{\cdot}D_2O$. *Phys. Rev. B* **2016**, *94*, No. 214405.
(34) Tian, W.; Cao, H. B.; Clune, A. J.; Hughey, K. D.; Hong, T.; Yan, J.-Q.; Agrawal, H. K.; Singleton, J.; Sales, B. C.; Fishman, R. S.; Musfeldt, J. L.; Fernandez-Baca, J. A. Electronic phase separation and magnetic-field-induced phenomena in molecular multiferroic $(ND_4)_2FeCl_5{\cdot}D_2O$. *Phys. Rev. B* **2018**, *98*, No. 054407.
(35) Bai, X.; Fishman, R. S.; Sala, G.; Pajerowski, D. M.; Garlea, V. O.; Hong, T.; Lee, M.; Fernandez-Baca, J. A.; Cao, H.; Tian, W. Magnetic excitations of the hybrid multiferroic $(ND_4)_2FeCl_5{\cdot}D_2O$. *Phys. Rev. B* **2021**, *103*, No. 224411.
(36) Rodríguez-Velamazán, J. A.; Fabelo, O.; Campo, J.; Millán, A.; Rodríguez-Carvajal, J.; Chapon, L. C. Magnetic-field-induced change of magnetoelectric coupling in the hybrid multiferroic $(ND_4)_2[FeCl_5D_2O]$. *Phys. Rev. B* **2017**, *95*, No. 174439.
(37) Li, S.; Fishman, R. S. Phase transitions of the ferroelectric $(ND_4)_2FeCl_5{\cdot}D_2O$ under magnetic field. *Phys. Rev. B* **2021**, *104*, No. L060407.
(38) Clune, A. J.; Nam, J.; Lee, M.; Hughey, K. D.; Tian, W.; Fernandez-Baca, J. A.; Fishman, R. S.; Singleton, J.; Lee, J. H.; Musfeldt, J. L. Magnetic field-temperature phase diagram of multiferroic $(NH_4)_2FeCl_5{\cdot}H_2O$. *npj Quantum Mater.* **2019**, *4*, 44.
(39) Lee, M. Magnetic phase diagram of $A_2[FeCl_5(H_2O)]$ (A = K, Rb, NH_4). *J. Magn. Magn. Mater.* **2022**, *555*, No. 169302.
(40) Hughey, K. D.; Lee, M.; Nam, J.; Clune, A. J.; O'Neal, K. R.; Tian, W.; Fishman, R. S.; Ozerov, M.; Lee, J. H.; Zapf, V. S.; Musfeldt, J. L. High-Field Magnetoelectric and Spin-Phonon Coupling in Multiferroic $(NH_4)_2[FeCl_5{\cdot}(H_2O)]$. *Inorg. Chem.* **2022**, *61*, 3434−3442.
(41) Clune, A.; Harms, N.; O'Neal, K. R.; Hughey, K.; Smith, K. A.; Obeysekera, D.; Haddock, J.; Dalal, N. S.; Yang, J.; Liu, Z.; Musfeldt, J. L. Developing the Pressure−Temperature−Magnetic Field Phase Diagram of Multiferroic $[(CH_3)_2NH_2]Mn(HCOO)_3$. *Inorg. Chem.* **2020**, *59*, 10083−10090.
(42) Zhou, H.; Ding, H.; Yu, Z.; Yu, T.; Zhai, K.; Wang, B.; Mu, C.; Wen, F.; Xiang, J.; Xue, T.; Wang, L.; Liu, Z.; Sun, Y.; Tian, Y. Pressure Control of the Structure and Multiferroicity in a Hydrogen-Bonded Metal-Organic Framework. *Inorg. Chem.* **2022**, *61*, 9631−9637.
(43) Mao, H. K.; Bell, P. M.; Shaner, J. W.; Steinberg, D. J. Specific volume measurements of Cu, Mo, Pd, and Ag and calibration of the ruby R1 fluorescence pressure gauge from 0.06 to 1 Mbar. *J. Appl. Phys.* **1978**, *49*, 3276−3283.
(44) Mao, H. K.; Xu, J.; Bell, P. M. Calibration of the ruby pressure gauge to 800 kbar under quasi-hydrostatic conditions. *J. Geophys. Res.* **1986**, *91*, 4673−4676.
(45) *PeakFit: Peak Separation and Analysis Software for Windows*; Jandel Scientific Software, 1995.
(46) Cotton, S. A.; Gibson, J. F. Spectroscopic studies of some aquo-complexes of Iron(III) and Indium(III). *J. Chem. Soc. A* **1971**, 1693−1696.
(47) Sharma, S. K.; Pandya, D. K. Laser-Raman spectra of crystalline $(NH_4)_2FeCl_5{\cdot}H_2O$, $K_2FeCl_5{\cdot}H_2O$ and $K_2FeCl_5{\cdot}D_2O$. *J. Inorg. Nucl. Chem.* **1974**, *36*, 1165−1166.
(48) Adams, D. M.; Lock, P. J. A survey study of the vibrational spectra of some aquo-halogeno-complexes. *J. Chem. Soc. A* **1971**, 2801−2806.
(49) Parker, S. F.; Shankland, K.; Spurnt, J. C.; Jayasooriya, U. A. The nine modes of complexed water. *Spectrochim. Acta A* **1997**, *53*, 2333−2339.
(50) McCarthy, P. J.; Walker, I. M. Water overtone and combination bands in the near-infrared spectrum of $M_2FeCl_5H_2O$ (M = Cs, K) at cryogenic temperatures. *Spectrochim. Acta Part A* **1983**, *39A*, 827−834.
(51) Piszczek, P.; Grodzicki, A.; Engelen, B. Infrared and Raman studies of water molecule normal vibrations in crystalline hydrates which form the chain structures. *J. Mol. Struct.* **2003**, *646*, 45−54.
(52) Brüning, D.; Fröhlich, T.; Langenbach, M.; Leich, T.; Meven, M.; Becker, P.; Bohatý, L.; Grüninger, M.; Braden, M.; Lorenz, T. Magnetoelectric coupling in the mixed erythrosiderite $[(NH_4)_{1-x}K_x]_2[FeCl_5(H_2O)]$. *Phys. Rev. B* **2020**, *102*, No. 054413.
(53) Verdal, N.; Udovic, T. J.; Rush, J. J.; Stavila, V.; Wu, H.; Zhou, W.; Jenkins, T. Low-temperature tunneling and rotational dynamics of the ammonium cations in $(NH_4)_2B_{12}H_{12}$. *J. Chem. Phys.* **2011**, *135*, No. 094501.
(54) Lacková, D.; Ondrejkovičová, I.; Koman, M. A new pathway of preparation and refined structure of $(NH_4)_2[FeCl_5(H_2O)]$. *Acta Chim. Slovaca* **2013**, *6*, 129−132.
(55) Falk, M.; Huang, C.-H.; Knop, O. Infrared studies of water in crystalline hydrates: $K_2FeCl_5{\cdot}H_2O$ (erythrosiderite) and related aquopentachloroferrates(III). *Can. J. Chem.* **1975**, *53*, 51−57.
(56) Yan, T.; Wang, K.; Tan, X.; Yang, K.; Liu, B.; Zou, B. Pressure-induced phase transition in N-H··· O hydrogen-bonded molecular crystal biurea: combined Raman scattering and X-ray diffraction study. *J. Phys. Chem. C* **2014**, *118*, 15162−15168.
(57) Wang, K.; Liu, J.; Yang, K.; Liu, B.; Zou, B. High-pressure-induced reversible phase transition in sulfamide. *J. Phys. Chem. C* **2014**, *118*, 18640−18645.
(58) Aroyo, M. I.; Perez-Mato, J. M.; Orobengoa, D.; Tasci, E.; de la Flor, G.; Kirov, A. Crystallography online: Bilbao crystallographic server. *Bulg. Chem. Commun.* **2011**, *43*, 183−197.
(59) Aroyo, M. I.; Perez-Mato, J. M.; Capillas, C.; Kroumova, E.; Ivantchev, S.; Madariaga, G.; Kirov, A.; Wondratschek, H. Bilbao crystallographic server I: databases and crystallographic computing programs. *Z. Kristallogr.* **2006**, *221*, 15−27.
(60) Aroyo, M. I.; Kirov, A.; Capillas, C.; Perez-Mato, J. M.; Wondratschek, H. Bilbao crystallographic server II: represenations of cryallographic point groups and space groups. *Acta Crystallogr., Sect. A* **2006**, *A62*, 115−128.
(61) Aoyama, T.; Yamauchi, K.; Iyama, A.; Picozzi, S.; Shimizu, K.; Kimura, T. Giant spin-driven ferroelectric polarization in $TbMnO_3$ under high pressure. *Nat. Commun.* **2014**, *5*, 4927.

https://doi.org/10.1021/acs.inorgchem.4c00403
Inorg. Chem. 2024, 63, 11021−11029